# Impact of communal irrigation on the 2018 Palu earthquake-triggered landslides

Ian M. Watkinson* & Robert Hall

SE Asia Research Group, Department of Earth Sciences, Royal Holloway University of London, Egham, Surrey TW20 0EX, United Kingdom *ian.watkinson@rhul.ac.uk

# Impact of communal irrigation on the 2018 Palu earthquake-triggered landslides

Ian M. Watkinson* & Robert Hall

SE Asia Research Group, Department of Earth Sciences, Royal Holloway University of London, Egham, Surrey TW20 0EX, United Kingdom *ian.watkinson@rhul.ac.uk

**Anthropogenic changes to the environment can enhance earthquake-triggered landslides, yet their role in earthquake disasters is often overlooked. Coseismic landslides frequently involve liquefaction of granular materials, a process that reduces shear strength and facilitates downslope motion even on gentle slopes. Irrigation systems can increase liquefaction susceptibility and compromise otherwise stable slopes. Here we investigate devastating landslides that affected Palu, Indonesia, during the 28$^{th}$ September 2018 $M_w$7.5 earthquake. We document fields and buildings translated over 1 km down slopes of less than 2° and show landslides were limited to irrigated ground. A liquefied detachment was rooted upslope in a conveyance canal that supplied water to the irrigation network. A strong correlation between landslide displacement, irrigation infrastructure and the highest slopes (≥1.5°), suggests a causative mechanism that should provoke urgent assessment of gently sloping irrigated terrain elsewhere in Sulawesi and in tectonically active areas worldwide.**

While population growth and urbanisation expose more people to earthquake disasters generally[1,2], anthropogenic modification of the environment can increase the risk of specific earthquake hazards. Landslides, the most common secondary effect of earthquakes[3], are sensitive to anthropogenic changes to land-use[4,5], climate[6], topography[7,8] and hydrology[9],

47 especially when coupled with strong seismicity[10,11]. Understanding earthquake-triggered
48 landslides in modified environments is vital to ensure appropriate measures are taken during
49 reconstruction and to identify vulnerable areas elsewhere[12].
50 The Indonesian city of Palu, Central Sulawesi, has been identified as vulnerable to
51 earthquakes triggered by the Palu-Koro Fault, which passes immediately west of the urban
52 centre[13,14,15,16,17] (Fig. 1a,b). Sited within a narrow valley facing an elongate bay, the city is
53 especially vulnerable to tsunami and landslides[17,18,19,20]. On 28th September 2018, a $M_w$7.5
54 earthquake centred 85 km north of Palu[21,22] initiated a disaster that left 2,081 people dead,
55 1,309 missing and 206,494 displaced[23]. Three main landslides, of 0.3-1.4 $km^2$ surface area
56 and 1.1 km maximum displacement, destroyed suburban areas on gently sloping alluvial fans:
57 Balaroa in the west, Petobo and Sidera in the east (Fig. 1c). The eastern landslides were tied
58 to a conveyance canal designed to enhance irrigated rice production in Palu valley[24,25], which
59 is dry (547-726 mm/a rainfall) compared to surrounding mountains (up to 3997 mm/a)[18].
60 We present analysis of the eastern landslides and irrigation system, based on satellite
61 imagery. The imagery quality, dense human development and raft-like behaviour of landslide
62 blocks allow assessment of irrigation's role in Indonesia's most deadly coseismic landslides.
63 All significant (≥10 m displacement) landslides identified within Palu valley are marked in
64 Fig. 1c. The only landslide we do not consider here is Balaroa, because it was isolated, much
65 smaller than the eastern landslides (0.38 $km^2$), adjacent to the surface rupture and not
66 associated with a major irrigation system (Supplementary Discussion 1.1).

67 **Landslide genesis and kinematics**

68 Three hours after a $M_w$6.1 foreshock, the 28th September 2018 $M_w$7.5 mainshock ruptured
69 >180 km southwards through Palu (Fig. 1b), in places at supershear velocity[21,22]. Surface
70 offset peaked at about 8 m[21] along the sinistral Palu-Koro Fault, which bisects Central
71 Sulawesi. The 500 km-long fault slips at 35-39 mm/yr[13,14], has a shallow locking depth[14] and

clear geomorphic expression[13,17,26], particularly along a topographic scarp west of Palu[13]. Significant earthquakes in the region (12th January 1927; 20th May 1938; 14th August 1968; 1st January 1996[27,28]) caused strong ground motions and tsunami[19,29], but there are no reports of landslides similar to those of 2018.

Here we use very high resolution DigitalGlobe natural colour satellite imagery acquired on 20th February 2018 and on 2nd October 2018, four days after the earthquake (see Methods and Supplementary Figs. 1-3), to evaluate the relationship between: (a) a lateral spread landslide with >150 m displacement (Lolu landslide); (b) two lateral spread/translational landslides with >1 km displacement and cogenetic debris flows (Petobo and Sidera landslides); (c) zones of distributed lateral spreading; and (d) irrigation infrastructure (Fig. 2a, Methods and Supplementary Fig. 4). Landslide fractures were interpreted and objects recognisable in pre- and post-earthquake imagery tracked to map displacement (Fig. 2b-d, Methods and Supplementary Figs. 5-7). We assume tracked objects record landslide motions not superficial liquefied soil flow because of the consistent displacement field and relationship to landslide fractures. Mapped fractures lie 7-8 km east of the surface rupture, and show no signs of being tectonic in origin. Displacement was downslope, orthogonal to tectonic motion, and interpreted to have been gravity driven. Precipitation before the earthquake was average to low (see Supplementary Discussion 1.2).

Lolu landslide (Fig. 3a) exemplifies a simple lateral spread above a weak detachment[30,31]. Maximum displacement is 157 m. An arcuate crown fault system formed in Lolu village at 73 m elevation, the landslide terminates in a plantation 760 m west at 63 m elevation, giving an average slope of 0.75°. Above the crown, arcuate cracks extend east to the conveyance canal. The crown is a curvilinear array of normal faults, with individual heaves of ~2 m. Discrete hangingwall and footwall cutoffs suggest a coherent surface layer. Lateral margins are zones of strike-slip (Fig. 2b), imbricate thrusts characterise the toe. Light-coloured lobes along

fractures may be liquefied sediment escaping from the basal detachment, and ponded water and sand blows in adjacent fields suggest widespread liquefaction (Supplementary Figs. 4 and 8).

Petobo landslide (Fig. 3b) is kinematically similar to Lolu. It descends a 1.2° slope from 83 m to 38 m elevation along its 2,190 m length. A scalloped crown preserves individual fault heaves up to 20 m (Fig. 2c). Maximum horizontal translation is 1,096 m – displacement increases systematically from crown and toe to a well-defined peak, lending confidence to our observed maximum (Supplementary Figs. 6 and 7). The landslide's centre, stripped of recognisable objects, represents the exhumed basal detachment. The toe thrust (Fig. 2d) is pinned in an urban area, beyond which there is negligible strain. Cogenetic debris flows mark the southern margin and sand lobes mark the northern strike-slip margin.

Sidera landslide (Supplementary Fig. 4), similar to Lolu and Petobo upslope, has evolved into a debris flow downslope where it merges with Paneki River. However, a partially preserved thrust belt at 57 m elevation, 26 m below and 1,950 m WSW of the crown, suggests a landslide slope of 0.76°. Maximum displacement of a recognisable object is 1,099 m (Supplementary Fig. 7), though that object may have been partly moved by entrainment in the debris flow.

Lolu, Petobo and Sidera landslides define peaks in a map of displacement based on tracked objects (Fig. 4a and Methods). Additional significant ground displacement around Lolu is expressed by high displacement lobes and nested arcuate cracks. South of Sidera, distributed displacement is associated with widely-spaced fractures and crown cracks. Water ponding and sand blows in both areas suggests extensive liquefaction (Supplementary Fig. 4).

**Irrigation infrastructure**

There is a striking spatial coincidence between the landslides and the irrigation system that supplies Palu valley (Fig. 2, Methods and Supplementary Figs. 9 and 10). Irrigation water is

carried northwards along a 15-25 m wide conveyance canal that traverses west-dipping alluvial fans south of Palu. Near Palu airport the canal turns 90° and narrows as it enters the city. Six 3 m wide secondary canals and many smaller channels flow downslope from >21 engineered turnouts along the damaged section of the canal. Water enters fields via distribution channels fed by concrete division boxes or artisanal systems. The density of irrigation infrastructure may be a proxy for shallow water infiltration. Vegetation is healthy in the irrigated area and sparse upslope of the canal (Methods and Supplementary Fig. 11).

The conveyance canal forms the upslope limit of all significant landslide faults and surface displacements (Fig. 4a), most crown faults are localised within or at most 125 m west of the canal (Fig. 2 and Supplementary Figs. 4 and 10). Average turnout frequency decreases from one per 210 m at Petobo, to one per 320 m at Lolu/Sidera, to just one per 440 m south of Sidera. Additionally, Petobo landslide is localised where a secondary canal from the SE terminates in a distribution system, and along the axis of the canal to the city centre (Fig. 3b). Small fracture systems upslope of the conveyance canal near Biromaru and the airport are not associated with significant surface displacement.

Lolu landslide's crown lies 620 m west of the conveyance canal; however, it nucleated along a smaller channel within Lolu village at the termination of a 3 m wide secondary canal (Fig. 3a). The crown is delimited by irrigation turnouts and a concrete division box.

**Landslide controls**

Landslide activity was limited to irrigated terrain mostly sloping ≤ 1.5°. Slopes above the irrigation network did not fail, despite being steeper, indicating irrigation water was a more important control on landsliding than slope alone. However, steeper topography (1.5°-4.0°) close to the main conveyance canal at the top of Petobo and Sidera landslides, may have precipitated localised failure where irrigation water was also present.

To evaluate landslide controls, we conducted correlation coefficient and principal component analysis (PCA) using 12 parameters measured across the study area and in ten 0.25 x 8 km swaths (Fig. 4b, Methods and Supplementary Figs. 11 and 12). Parameters included displacement, slope, aspect, vegetation and distance from features such as the earthquake epicentre, surface rupture, canal and irrigation nodes (e.g. turnouts). For landslide displacement, the strongest correlations (0.34-0.41) are displacement azimuth and distances to the canal and irrigation nodes. These correlations rise to 0.66-0.94 in swath 3 (Petobo landslide) and 0.71-0.73 in swath 6 (Lolu landslide). In all landslide swathes, irrigation parameters (distance to canal, nodes and other channels) correlate strongly with ground displacement (Fig. 4c, Supplementary Tables 1-11). Slope is the next most correlated parameter. PCA reveals the first principal component (PC1) contains 62.6% of variance, dominated by irrigation parameters. PC2 (15.8% of variance) is dominated by geographic parameters (distance to Palu River, surface rupture). PC3 (6.1% of variance) is dominated by landslide parameters (displacement amount, azimuth). A composite RGB image of the most correlated parameters plus maps highlighting slope ≥1.5° and areas >250 m from irrigation channels (Fig. 4b) shows bright regions (A,B,C) representing coincident correlation peaks within the main landslides. Only one site of high displacement (D) lies outside the strongly correlated area. Here, landsliding may be in response to initial failure at A, supported by curvature of the crown faults and WSW-directed displacement vectors in this region.

Landslides on gentle slopes can be caused by cyclic shearing-induced liquefaction of water saturated, unconsolidated granular materials[32,33,34]. Liquefaction increases pore fluid pressure such that the material loses shear strength and cannot support topography. Young, layered, unconsolidated granular sediments below the water table are most susceptible to liquefaction[35]. Eastern Palu valley is underlain by Quaternary alluvial fans[36] sourced from nearby crystalline rocks[37]. Where the water table is locally elevated by irrigation, the alluvial

fans satisfy all conditions for liquefaction. Liquefaction can also be triggered by compressional loading from upslope collapse[38] – a feedback that may explain higher displacements below the steeper initiation points. Fluidised sand along landslide margins, water ponding and sand blows (see Methods and Supplementary Figs. 4 and 8), indicate an important role for coseismic liquefaction within the irrigated area only. Additionally, shallow water infiltration can introduce mechanical heterogeneity, promoting gentle slope failure[39], suggested by exposure of a stratiform basal detachment in Petobo and Sidera landslides. Turnagain Heights (Anchorage) is the classic example of liquefaction-induced lateral spread, formed during the 1964 M8.5 Alaskan earthquake. A 0.5 $km^2$ area experienced 610 m displacement above liquefied sands[40]. Contemporary accounts[40] suggest morphological similarities to the Palu landslides, though at 1.4 $km^2$ surface area and 1096 m displacement, the Petobo landslide alone may be the largest lateral spread ever documented.

## Implications for landslide mitigation

We conclude that naturally metastable alluvial fans surrounding Palu city were compromised by an elevated water table caused by water infiltration downslope of the conveyance canal and irrigation infrastructure. Irrigation water enhanced mechanical heterogeneity and liquefaction susceptibility, leading to catastrophic failure during the Mw7.5 earthquake. A critical condition for the two very long run-out landslides was the coincidence of the conveyance canal and topographic slopes $\geq 1.5°$.

The area south of Sidera (location E, Fig. 4b) requires further investigation since, like Petobo and Sidera, it is marked by widespread liquefaction and slopes $\geq 1.5°$ adjacent to the canal, yet surface displacement was small. Other areas of concern include the wider Lolu region; upper parts of Petobo and Sidera landslides now with free surfaces against topographic depressions; and irrigated areas of southern Palu valley.

Irrigation-linked landslides have been documented before[9,41,42,43]. Loess collapse below a canal during the 1989 Dushanbe earthquake, Tajikistan, was similar to the 2018 Palu landslides in scale, topography, crown fault arrangement, exposure of detachment surfaces and associated debris flows[44]. Palu's landslides thus provide further warning that irrigation in seismically active areas may critically undermine very gentle slopes, particularly in urban settings. Irrigation systems are widespread in seismically active and increasingly urbanised parts of Indonesia[45], Myanmar[46] and beyond[47]. Mitigation strategies to prevent future similar landslides might include: minimising water infiltration in areas of steepest slope by utilising dendritic secondary canals originating from fewer turnouts; building tiered, parallel conveyance canals to result in smaller, spaced perturbations of the water table; staggering land use (agriculture, forestry, urban areas) so dry/root-stabilised soil punctuates water saturated areas; and driving stabilising piles across strata of high liquefaction susceptibility in particularly vulnerable urban areas.

## References


1. Bilham, R. Lessons from the Haiti earthquake. *Nature* **463,** 878-879 (2010).
2. Holzer, L. T. & Savage, J. C. Global Earthquake Fatalities and Population. *Earthquake Spect.* **29,** 155-175 (2013).
3. Marano, K. D., Wald, D. J. & Allen, T. I. Global earthquake casualties due to secondary effects: a quantitative analysis for improving rapid loss analyses. *Nat. Haz.* **52,** 319-328 (2010).
4. Alcántara-Ayala, I., Esteban-Chávez, O. & Parrot, J. F. Landsliding related to land-cover change: A diachronic analysis of hillslope instability distribution in the Sierra Norte, Puebla, Mexico. *Catena* **65,** 152-165 (2006).

5. Pisano, L. et al. Variations in the susceptibility to landslides, as a consequence of land cover changes: A look to the past, and another towards the future. *Sci. of the Total Env*. **601-602,** 1147-1159 (2017).

6. Sangelantoni, L., Gioia, E. & Marincioni, F. Impact of climate change on landslides frequency: the Esino river basin case study (Central Italy). *Nat. Haz*., **93,** 849-884 (2018).

7. Barnard, P. L., Owen, L. A., Sharma, M. C. & Finkel, R. C. Natural and human-induced landsliding in the Garhwal Himalaya of northern India. *Geomorph*. **40,** 21-35 (2001).

8. Hearn, G. J. & Shakya, N. M. Engineering challenges for sustainable road access in the Himalayas. *Quat. J. of Eng. Geol & Hydrogeol*. **50,** 69-80 (2017).

9. Zhang, D., Wang, D., Luo, C., Chen, J. & Zhou, Y. A rapid loess flowslide triggered by irrigation in China. *Landslides* **6,** 55-60 (2009).

10. Tanyaş, H. et al. Presentation and Analysis of a Worldwide Database of Earthquake-Induced Landslide Inventories. *J. of Geophys, Res: Earth Surface* **122,** 1991-2015 (2017).

11. Owen, L. A. et al. Landslides triggered by the October 8, 2005, Kashmir earthquake. *Geomorph*. **94,** 1-9 (2008).

12. Keefer, D. K. Investigating landslide caused by earthquakes – a historical review. *Surv. Geophys*. **23,** 473–510 (2002).

13. Bellier, O. et al. High slip rate for a low seismicity along the Palu-Koro active fault in central Sulawesi (Indonesia). *Terra Nova* **13,** 463-470 (2001).

14. Socquet, A. et al. Microblock rotations and fault coupling in SE Asia triple junction (Sulawesi, Indonesia) from GPS and earthquake slip vector data. *J. Geophys. Res*. **111,** B08409 (2006).

15. Thein, P. S. et al. Site response characteristics of H/V spectrum by microtremor single station observations at Palu city, Indonesia. *J. SE Asian Appl. Geol*. **5,** 1-9 (2013).

16. Cipta, A. et al. in *Geohazards in Indonesia: Earth Science for Disaster Risk Reduction* (eds Cummins, P. R. & Meilano, I.) 133–152 (Geological Society Special Publications Vol. 441, Geological Society, London, 2017).

17. Watkinson, I. M. & Hall, R. in *Geohazards in Indonesia: Earth Science for Disaster Risk Reduction* (eds Cummins, P. R. & Meilano, I.) 71-120 (Geological Society Special Publications Vol. 441, Geological Society, London, 2017).

18. Metzner, J. Palu (Sulawesi): Problems of land utilisation in a climatic dry valley on the equator. *Erdkunde* **35,** 42-54 (1981).

19. Pelinovsky, E., Yuliadi, D., Prasetya, G. & Hidayat, R. The 1996 Sulawesi tsunami. *Nat. Haz*. **16,** 29-38 (1997).

20. Sutapa, I. W. & Galib, I. M. Application of non-parametric test to detect trend rainfall in Palu watershed, Central Sulawesi, Indonesia. *Int. J. Hydrol, Sci. & Tech*. **6,** 238-253 (2016).

21. Socquet, A., Hollingsworth, J., Pathier, E. & Bouchon, M. Evidence of supershear during the 2018 magnitude 7.5 Palu earthquake from space geodesy. *Nat. Geosci*. **12,** 192-199 (2019).

22. Bao, H. et al. Early and persistent supershear rupture of the 2018 magnitude 7.5 Palu earthquake. *Nat. Geosci*. **12,** 200-205 (2019).

23. *Situation update No.15 – final. M7.4 earthquake & Tsunami Sulawesi, Indonesia* (ASEAN Coordinating Centre for Humanitarian Assistance on Disaster Management, accessed 25 November 2018); https://reliefweb.int/report/indonesia/aha-centre-situation-update-no-15-final-m-74-earthquake-and-tsunami-sulawesi

24. Weber, R. Kreisel, W. & Faust, H. Colonial Interventions on the Cultural Landscape of Central Sulawesi by "Ethical Policy": The Impact of the Dutch Rule in Palu and Kulawi Valley, 1905–1942. *Asian J. of Soc. Sci*. **31,** 398-434 (2003).

25. Keil, A., Zeller, M., Wida, A., Sanim, B. & Birner, R. What determines farmers' resilience towards ENSO-related drought? An empirical assessment in Central Sulawesi, Indonesia. *Climatic Change* **86,** 291-307 (2008).

26. Hamilton, W. Tectonics of the Indonesian region. *U.S. Geological Survey Professional Paper 1078,* 345 pp. (1979).

27. Dunbar, P. K., Lockridge, P. A. & Whiteside, L. S. *Catalog of Significant Earthquakes 2150 B.C. – 1991 A.D.* (National Geophysical Data Center, Boulder, Colorado 1992).

28. Hamzah, L., Puspito, N. T. & Imamura, F. Tsunami catalog and zones in Indonesia. *J. of Nat. Dis. Sci*. **22,** 25-43 (2000).

29. Prasetya, G. S., de Lange, W. P. & Healy, T. R. The Makassar Strait tsunamigenic region, Indonesia. *Nat. Hazards* **24**, 295-307. (2001).

30. Varnes, D. J. in *Landslides, Analysis and Control, Special Report 176* (eds Schuster, R. L. & Krizek, R. J.) 11-33 (Transport Research Board, National Academy of Sciences, Washington, DC, 1978).

31. Youd, T. L. & Garris, C. T. Liquefaction-induced ground-surface disruption. *J. of Geotech. Eng*. **121,** 805-809 (1995).

32. Bartlett, S. F. & Youd, T. L. Empirical analysis of horizontal ground displacement generated by liquefaction-induced lateral spreads. *National Centre for Earthquake Research Technical Report NCEER-92-0021,* 118 pp. (1992).

33. Glass, C. E., in *Interpreting Aerial Photographs to Identify Natural Hazards* 67-95 (Elsevier, Amsterdam, 2013).

34. Imtiyaz A. Parvez & Rosset, P. in *Earthquake Hazard, Risk and Disasters* (ed Wyss, M.) 273-304 (Elsevier, Amsterdam, 2014).

35. Youd, L. T. in *International Handbook of Earthquake and Engineering Seismology, 81B* (eds Lee, W. H. K., Kanamori, H., Jennings, P. C. & Kisslinger, C.) 1159-1173 (Academic Press, Cambridge, Massachusetts, 2003).

36. Sukamto, R. et al. *Reconnaissance Geological Map of the Palu Quadrangle, Sulawesi* (Geological Research and Development Centre, Jakarta, 1973).

37. van Leeuwen, T. M. & Muhardjo. Stratigraphy and tectonic setting of the Cretaceous and Paleogene volcanic–sedimentary successions in northwest Sulawesi, Indonesia: Implications for the Cenozoic evolution of Western and Northern Sulawesi. *J. of Asian Earth Sci*. **25,** 481–511 (2005).

38. Iverson, R. M. et al. Landslide mobility and hazards: implications of the 2014 Oso disaster. *Ear. Plan. Sci. Lett*. **412,** 197-208 (2015).

39. Moayedi, H. et al. Preventing landslides in times of rainfall: case study and FEM analyses. *Disaster Prev. & Manage*. **20,** 115-124 (2011).

40. Bolton Seed, H. & Wilson S. D. The Turnagain Heights landslide, Anchorage, Alaska. *J. Soil Mech. Found. Div.* **93,** 325-353 (1967).

41. Derbyshire, E., Meng, X. M. & Dijkstra, T. A. *Landslides in the Thick Loess Terrain of North-West China* (Wiley, Chichester, 2000).

42. Ishihara, K. et al. Geotechnical aspects of the June 20, 1990 Manjil earthquake in Iran. *Soils & Foundations* **32,** 61-78 (1992).

43. Evans, S.G. et al. Landslides triggered by the 1949 Khait earthquake, Tajikistan, and associated loss of life. *Eng. Geol*. **109,** 195-212 (2009).

44. Ishihara, K., Okusa, S., Oyagi, N. & Ischuk, A. Liquefaction-induced flow slide in the collapsible loess deposit in Soviet Tajik. *Soils & Foundations* **30,** 73-89 (1990).

45. Sato, S., Yamaji, E. & Kuroda, T. Strategies and engineering adaptions to disseminate SRI methods in large-scale irrigation systems in Eastern Indonesia. *Paddy Water Env*. **9,** 79-88 (2011).

46. Naing, M. M. in *Proceedings of the Regional Workshop on the Future of Large Rice-Based Irrigation Systems in Southeast Asia* 120-130 (Vietnam Institute for Water Resources Research, Ho Chi Minh City, 2005).

47. Mukherji, A. et al. Revitalizing Asia's irrigation: to sustainably meet tomorrow's food needs *(International Water Management Institute, Colombo; Food and Agriculture Organization of the United Nations*, Rome, 2009).

48. *201809281002A Minahassa Peninsula, SUL* (Global Centroid-Moment-Tensor Project, accessed 25 November 2018); https://www.globalcmt.org/

49. Dziewonski, A. M., Chou, T.-A. & Woodhouse, J. H. Determination of earthquake source parameters from waveform data for studies of global and regional seismicity, *J. Geophys. Res*. **86,** 2825-2852 (1981).

50. Ekström, G., Nettles, M. &. Dziewonski, A. M. The global CMT project 2004-2010: Centroid-moment tensors for 13,017 earthquakes, *Phys. Earth Planet. Inter*. **200-201,** 1-9 (2012).

Correspondence and requests for materials should be addressed to I. M. W. at ian.watkinson@rhul.ac.uk

**Acknowledgements**

We are grateful to Elizabeth L. Chamberlain and two anonymous reviewers for their constructive feedback.

## Author contributions

I. M. W. carried out the satellite image interpretation, wrote the manuscript and created the figures. R. H. contributed to image interpretation, worked on image georeferencing, processed the TanDEM elevation model and commented on the manuscript.

## Competing Financial Interests

The authors declare no competing interests.

## Figure Legends

**Fig. 1: Regional context and overview. a,** Location of Sulawesi, Indonesia. **b**, Central Sulawesi, showing the Palu-Koro Fault, Palu city, the two largest earthquakes of 28th September 2018[48,49,50] and the $M_w$7.5 surface rupture, after ref. [21]. **c,** Overview of the earthquake-triggered landslides (black areas) of the Palu valley, including Balaroa in the west, and Petobo and Sidera in the east. The main rivers and irrigation channels are shown. Base map is from 12.5 m TanDEM-X topographic data, 2018 surface rupture is drawn after ref. [21].

**Fig. 2: Landslides and irrigation, eastern Palu valley. a,** Simplified interpretation of landslide domains, landslide-related fractures, urban areas, irrigation channels, topographic contours (from 12.5 m TanDEM-X). Location in Fig. 1c. See Methods for description and Supplementary Fig. 4 for full interpretation. **b,** Northern strike-slip margin, Lolu landslide. Housing estate (red roofs) was originally square in plan. **c,** Extensional domain of Petobo landslide, detaching along the conveyance canal. **d,** Toe thrust system of Petobo landslide, highlighting shortening and coherent thrust slices. Representative tracked objects circled in yellow, displacement in metres. Locations in Figs. 2a. and 3. Imagery ©2018 Google and DigitalGlobe.

**Fig. 3: Structural maps of two representative landslides. a,** Lolu landslide, showing pre-earthquake irrigation infrastructure, roads, buildings and topographic contours. Post-

earthquake roads and building positions shown in darker grey. **b,** Petobo landslide, showing pre-earthquake irrigation elements, urban areas and topographic contours. See Supplementary Fig. 6 for individual building tracking in Petobo landslide. In both maps, representative displacement vectors are shown at the same scale as the map. Map locations shown in Fig. 2a. Full vector dataset shown in Supplementary Fig. 7.

**Fig. 4: Landslide displacement and controlling parameters. a,** Ground displacement (black dots: observation points) and irrigation infrastructure. **b,** The wider irrigated area (extent in Fig. 1c), combining five highly correlated parameters: (i) RGB image of displacement (red), distance from irrigation nodes (green) and distance downslope of conveyance canal (blue); (ii) slopes ≥ 1.5° (white), < 1.5° (black); (iii) regions >250 m from irrigation channels/rivers (yellow). Strong correlations expressed by bright areas (A, B, C). D: anomalously high displacement, E: anomalously low displacement. **c,** Absolute correlation coefficients between displacement and 11 other parameters for ten 0.25 x 8 km east-west swaths.

## Additional information

Supplementary information is available for this paper.

# Impact of communal irrigation on the 2018 Palu earthquake-triggered landslides

Ian M. Watkinson* & Robert Hall

SE Asia Research Group, Department of Earth Sciences, Royal Holloway University of London, Egham, Surrey TW20 0EX, United Kingdom *ian.watkinson@rhul.ac.uk

## Methods

**Data sources.** This study is based on two very high resolution 8-band panchromatic natural colour satellite images from DigitalGlobe[51] that cover the study area before and after the 28th September 2018 earthquake (Supplementary Fig. 1a). Images were acquired by the WorldView-4 satellite, and have variable spatial resolution, expressed as ground sample distance (GSD). Off-nadir angle (ON) is less than 24° in all scenes. The main pre-earthquake image was acquired on 20th February 2018 (scene ID: 1030010078CD4A00, GSD: 0.56 m, ON: 18.5°), and the post-earthquake image was acquired on 2nd October 2018 (scene ID: 1040010042376D00, GSD: 0.31 m, ON: 2.3°). Additional scenes acquired on 26th September 2017 (scene ID: 1030010073524100, GSD: 0.51 m, ON: 18.5°), 5th August 2017 (scene ID: 103001006F222600, GSD: 0.54 m, ON: 23.7°), and 26th February 2011 (source not known) were used in places to help map the pre-earthquake irrigation network. DigitalGlobe imagery was accessed using freely available Google Earth Pro software (https://www.google.com/earth/download) during October-November 2018. Scenes were viewed from directly above and terrain modelling was disabled to minimise interpreter errors related to perception and intuitive responses[52]. In addition, Google Street View (Supplementary Fig. 1b) was used to inspect pre-earthquake details of the irrigation infrastructure adjacent to main roads and to help identify the pre-earthquake location of

translated buildings. General observations of the irrigation infrastructure and the geology of the alluvial fans were made during fieldwork in 2009, 2010 and 2011. Pre-earthquake vegetation/moisture indices were mapped using Sentinel 2B satellite imagery acquired on 27th September 2018, in green/red/near infra-red bands 3 to 8 (central wavelengths 559 to 833 nm). Bands have 10-20 m spatial resolution[53]. Sentinel data were processed using ArcGIS software. We used topographic data from the German Aerospace Center's TanDEM-X satellite, which flew alongside the TerraSAR-X satellite to produce a high resolution global digital elevation model (DEM) by synthetic aperture interferometry[54]. The DEM has 0.4 arcseconds (~12 m) horizontal resolution and 2 m vertical accuracy where slope is < 20%. Full-resolution TanDEM-X data have been available for scientific use upon application since 2016[53], and a 90 m derivative has been freely available via the German Aerospace Centre since 2018: (https://geoservice.dlr.de/web/dataguide/tdm90/). We were awarded use of four ~12 m resolution 1°x1° tiles centred on 120°E, 1°S that cover Palu and Central Sulawesi. Shaded relief images and topographic contours used in the figures were derived from the TanDEM-X data. All geospatial data were processed in ArcGIS software and projected to a UTM zone 50S coordinate system, WGS1984 datum and Transverse Mercator projection.

**Positional accuracy of interpreted images.** Horizontal positional accuracy in Google Earth is often poorly constrained; estimates range from 39.7 m RMSE (root mean square error) in 2008[55] to 1.80 m in 2013[56] and ~1 m in 2015[57] for the natural colour imagery, and 2.64 m RMSE for the terrain model[58]. Digital Globe[51] report <5 m positional accuracy for their WorldView-4 satellite imagery. To test the positional accuracy of the two main images used they were calibrated against an independently acquired Global Positioning System (GPS) track (Supplementary Fig. 2). A track acquired using a Garmin Oregon 550T handheld GPS receiver was selected because it crossed the study area, including regions of low deformation, broadly from NW to SE. The track was acquired during fieldwork on 25th September 2010,

driving from north to south on the left side of the road from Palu to south of Sidera. From points placed at 100 m intervals along the track, offset from the centreline of the left-hand carriageway was measured in N-S and E-W directions. For the post-earthquake image, calibration measurements were only made where landslide displacement was <3 m – in most places along the GPS track landslide displacement was negligible. In all cases the GPS tracks are a good fit to the imagery, considering inherent GPS positional uncertainty, plotting on or very close to the road. For the 20$^{th}$ February 2018 scene, mean offset is 5.9 m east, standard deviation (SD) is 2.14 m (n=96); and 3.94 m north, SD 1.13 m (n=32). For the 2$^{nd}$ October 2018 scene, mean offset is 0.28 m west, SD 1.46 m (n=60); and 0.28 m south, SD 0.68 m (n=32) (Supplementary Fig. 3). This test shows that the post-earthquake imagery has a mean positional accuracy with respect to the GPS network close to the image's GSD (0.31 m). The pre-earthquake imagery is systematically offset to the NE by about 10 times its GSD.

For this study, positional consistency between satellite scenes is more important than high accuracy on a global framework. The GPS track test highlights a systematic positional offset of the pre-earthquake imagery accessed via Google Earth at the time of analysis, which is not present in the post-earthquake imagery. To ensure landslide displacements are considered within a fixed local reference frame, a grid of 12 tracked objects was picked on the upper alluvial fan east of the irrigation canal, away from all observed landslide activity. These objects were widely and evenly spaced, and selected because they could be tracked with confidence in both pre- and post-earthquake satellite images and were far from any landslide-related features. All 12 objects showed a systematic offset of the pre-earthquake image towards the ENE with respect to the post-earthquake image (mean azimuth 073°, SD 4.45°). Offset ranged from 3.46 m to 7.16 m (mean 5.45 m, SD 0.99 m) east; and from 0.82 m to 2.60 m (mean 1.64 m, SD 0.43 m) north (Supplementary Fig. 2e,f). These values are similar to the independent GPS track offset, within SD (E-W) and slightly larger than SD (N-S).

To remove the systematic offset between landslide displacement vectors measured from the pre- and post-earthquake images, a correction vector composed of the inverse mean offset values from the 12-point reference frame, i.e. 5.45 m west and 1.64 m south, was applied to the start point of all measured displacement vectors (Supplementary Fig. 3c). This correction reduced displacement vectors in the stable eastern area and in the region downslope of the landslides to <2 m, which is close to the accuracy of the object picks. Corrected vectors were then plotted in ArcGIS and used to derive a displacement raster (Fig. 4a)

**Landslide-related structural mapping.** With the advent of very high resolution satellite and aerial imagery, it is possible to map landslide-related fissures and other earthquake-related structures remotely[59,60], a critical step towards understanding landslide evolution[61]. Landslide-related fractures at the surface are dominated by tensile cracks because of the low tensile strength of geomaterials, and can be recognised as dark lines in optical imagery[62]. Dilational tension gashes, shear fractures and larger structures analogous to normal, thrust and strike-slip faults[63,64] were mapped from the post-earthquake scene (Supplementary Fig. 4). Fractures appear as dark or light lines ~10-100 m long, sometimes arranged into hard-linked 'faults' ≤1.3 km long. They displace roads and boundaries and can be marked by light patches interpreted as sand blows. En-echelon arrays, wing cracks, relay ramps and tip splays help distinguish fractures from cultural linear features such as tracks. Comparison with pre-earthquake imagery helped to confirm an earthquake origin for very small or poorly imaged linear features. Structures were mapped as vector polylines directly in Google Earth, exported to KMZ format and imported into ArcGIS software. Picking accuracy is ± 1-5 m.

**Displacement measurement.** Finite displacement of the ground surface was measured by tracking the position of 8,737 objects recognisable in both pre- and post-earthquake satellite imagery (Supplementary Figs 5-7). Manual object tracking was employed because digital image correlation[65] breaks down in areas of extreme damage in the post-earthquake

scene[66,67]. Tracked objects included points with high X-Y positional certainty, mostly roof features (e.g. ridge/hip/valley line intersections), wall vertices, small building centrepoints, field boundary intersections, track/road intersections, small bridge abutments and if necessary small isolated trees. Distinctive objects or associations of objects chosen were those that could be recognised in both post- and several scenes of pre-earthquake imagery (Supplementary Figs. 5 and 6). Objects at ground level were preferentially picked to minimise parallax error related to satellite view angle. Tracked objects were picked with about 30-100 m X-Y spacing, higher in regions of change and around fractures and faults. Higher densities were also picked ~250 m either side of the main conveyance canal to maximise certainty about the location of displacement onset. Lower densities resulted from an absence of recognisable objects, for example in woodland and in the Sidera debris flow. Accuracy of tracking points is in principle the same as the satellite image minimum ground sample distance (0.31 m), but given issues of parallax, lighting variation and the vagary of features such as footpaths or road margins, accuracy is probably closer to ± 1 m. Accuracy in some areas of high displacement is locally worse, perhaps ± 5-10 m, where collapsed buildings can be identified only as associations of colour patches representing clusters of building materials. In such cases the mid-point of buildings and colour patches was picked. Lines linking the pre-earthquake position (start) and post-earthquake position (end) of each tracked object were drawn directly in Google Earth, exported to KMZ format and imported into ArcGIS software. For correlation coefficient and principal component analysis (Fig. 4b,c and Supplementary Figs. 11-12), an additional 631 displacement measurements were made in the wider study area. No significant ground displacement was observed beyond the focal study area, so the additional data was gathered at a coarser spacing of about 250 m. These data were processed as described above.

**Mapping of liquefaction features**. Liquefaction is commonly manifested as ejected sediment and water, areas of ground distortion, fissures and settlement[35,68,69]; these features are visible in high resolution satellite imagery. Ground and aerial photograph-based studies from the 2010-2011 Christchurch, New Zealand, earthquake sequence[70-72] were used as a reference for identifying liquefaction effects in the post-earthquake imagery of Palu. Ponded, ejected water appears as irregular, often rounded patches of uniformly dark colour usually with a concentric fringe of lighter colour. Mottling in fields is often associated with ponding, and may represent partially drained water ponds and patches of residual sediment or stressed vegetation. Discrete sand blows from fractures appear as pale yellow patches or fan-like flows. All liquefaction-related features were compared to pre-earthquake imagery (Supplementary Fig. 8), mapped as vector points directly in Google Earth, exported to KMZ format and imported into ArcGIS software for map production (Supplementary Fig. 4).

**Displacement raster.** Corrected displacement vectors based on traced objects were plotted as points at the origin (pre-earthquake) X-Y coordinates. A natural neighbour triangular irregular network (TIN) was produced based on values from the corrected displacement field, and this was used to produce a 5 m resolution gridded raster surface representing displacement (Fig. 4a). The raster's colourbar histogram was manually adjusted to emphasise variation in displacement above the ± 1 m picking accuracy and below the 25 m threshold where displacement becomes extreme.

**Slope and aspect rasters.** The TanDEM-X digital elevation model was used to derive topographic slope and aspect rasters. Processing included filtering to remove off-terrain objects (trees, buildings) using a search neighbourhood of 30 cells and a slope threshold of 1.5°, to produce a digital terrain model (DTM). The DTM was cleaned with a low-pass filter to remove high frequency noise. For the slope raster, additional processing included averaging each cell to the mean of a search radius of 2 cells (~24-25 m) to slightly smooth

anomalous high amplitude features (mainly cultural) remaining in the terrain without reducing resolution. A slope raster was derived from that output. For Fig. 4b, a binary colourbar was applied with a threshold of 1.5°.

**Irrigation network mapping.** The irrigation network (Supplementary Fig. 4) was mapped using the post-earthquake image, plus pre-earthquake images, particularly scenes acquired on 20th February 2018 and 26th September 2017, to fill gaps where the land surface was badly damaged. Positional accuracy is similar to that for structural picking (± 1-2 m) but may be slightly worse because of minor, uncorrected positional differences between the scenes used. The primary and all secondary conveyance canals, most significant distribution channels and much of the water control and monitoring infrastructure was mapped (Supplementary Fig. 9), but many smaller downslope features and channels were omitted because of their high density and difficulty distinguishing them in satellite imagery. Turnouts can be recognised as 9x3 m open-sided buildings on the west side of the main canal that house valve controls and culvert inlets which project into the canal. Downslope of the valve house, one or more 3 m wide conveyance canals or substantial distribution channels carries water westwards. Canal level checks are identified by slightly smaller open-sided buildings built adjacent to bridges across the canal. Distribution boxes can be recognised where conveyance canals or main distribution channels split into two or more distribution channels, and are marked by a small open-sided building containing valve controls. Ground truthing of mapped irrigation features was possible using road-level quasi-continuous photographic imagery accessible via Google Street View, packaged within Google Earth (https://www.google.com/earth/download). Google Street View imagery was acquired in the Palu region during December 2015, and allowed close inspection of 6 turnouts, 4 checks, 3 division boxes and one sluice in the landslide-affected area, as well as long sections of the main canal, distribution channels and the Sapu river weir in the south. Example imagery is included in Supplementary Fig. 9.

Drainage lines and points were traced directly in Google Earth, exported to KMZ format and imported into ArcGIS software.

**Spatial correlation and principal component analysis (PCA).** To evaluate the spatial correlation between landslide displacement and 11 other parameters derived from the area east of the Palu River, we used the PCA toolbox in ArcGIS. The toolbox produces covariance and correlation matrices, eigenvectors and the principal components that show variation in the dataset. PCA has been used to analyse interdependence in complex datasets[73], including geospatial data[74]. Each of the 12 parameters was normalised to a 12.5 m resolution raster scaled 0-1. For PCA, the 9.8 x 4.6 km detailed study area was expanded to 15.7 x 8.5 km, clipped in the west by the Palu River, which forms the ultimate downslope limit of the earthquake-triggered landsliding. PCA was applied to the full composite raster and individually to ten E-W swaths of 250 m width (Fig. 4b) that cross regions of high, low and negligible landslide activity. The 12 parameters (see Supplementary Fig. 11) were: **1: Displacement azimuth,** derived from the measured displacement vectors (000° - 359°) and recalculated such that 270° had a maximum value of 1, 000° and 180° became 0.5, and 090° became 0. A 12.5 m raster was generated from the interpolated data. **2: Displacement amount,** calculated from the measured displacement vectors. To normalise, displacements of <3 m were assigned a value of 0, to acknowledge the high measurement uncertainty in that population. Higher displacements were assigned as follows: 3-<4 m (0.1); 4-<5 m (0.2); 5-<6 m (0.3); 6-<8 m (0.4); 8-<10 m (0.5); 10-<12 m (0.6); 12-<14 m (0.7); 14-<16 m (0.8); 16-<18 m (0.9); >18 m (1.0). All displacements above 18 m resulted in surface breaks and building destruction, so a value of 1 indicates onset of significant landsliding. A 12.5 m raster was generated from the interpolated data. **3: Modified Soil-Adjusted Vegetation Index**, (MSAVI2) is a standard measure of vegetation cover and health corrected for soil exposure, using multispectral satellite imagery[75]:

$$MSAVI2 = \frac{(2 \text{ x NIR} + 1 - \sqrt{(2\,x\,NIR + 1)^2 - 8 \text{ x } (NIR - RED)})}{2}$$

where NIR = near infra-red band, and RED = red band. MSAVI2 was normalised so that 1=healthy vegetation and 0= no vegetation. We used Sentinel 2B scene S2B_MSIL1C_20180927T022319_N0206_R103_T50MRD_20180927T055542, acquired on 27th September 2018, the day before the Palu earthquake. Sentinel 2B bands 4 (red, 664.9 nm wavelength) and 8 (near infra-red, 832.9 nm wavelength) have spatial resolutions of 10 m. **4: Distance downslope of the conveyance canal,** used to generate a 12.5 m raster with values from 1 (closest) to 0 (farthest). All points upslope of the canal were assigned values of 0. **5: Distance from irrigation channels,** used to generate a 12.5 m raster with values from 1 (closest) to 0 (farthest). **6: Distance from earthquake epicentre** (0.256°S, 119.846°E) was used to generate a 12.5 m raster with values from 1 (closest) to 0 (farthest). **7: Distance downslope of major irrigation nodes** along the mapped irrigation system (e.g. turnouts, division boxes) was used to generate a 12.5 m raster with values from 1 (closest) to 0 (farthest). All points upslope of the conveyance canal were assigned values of 0. **8: Distance from the Palu River**, immediately west of the study area, was used to generate a 12.5 m raster with values from 1 (closest) to 0 (farthest). **9: Distance from the 2018 surface rupture**, digitised after ref. [21], was used to generate a 12.5 m raster with values from 1 (closest) to 0 (farthest). **10: Sentinel 2B bands 843.** Bands 8 (near infra-red, NIR), 4 (red) and 3 (green) from Sentinel 2B scene S2B_MSIL1C_20180927T022319_N0206_R103_T50MRD_20180927T055542 were combined to generate a greyscale image, used to generate a 12.5 m raster with values from 1 (high NIR values) to 0 (high green values). **11: TanDEM-X topographic aspect,** the processed digital terrain model was used to generate a 12.5 m aspect raster with values from 1 (south) to 0 (north). **12: TanDEM topographic slope,** the processed digital terrain model

was used to generate a 12.5 m slope raster with values from 1 (19°) to 0 (0°). Full results of the correlation coefficient and principal component analysis are presented in Supplementary Tables 1-11. Correlation coefficients between displacement and the other 11 parameters within each of the ten swaths were used to produce the graph in Fig. 4c. Graphical representations of principal components 1, 2 and 3 are presented in Supplementary Fig. 12, alongside a composite RGB raster of all three.

**Data availability.**

Geospatial data generated during this project, including landslide displacement measurements, liquefaction indicators and digitised irrigation infrastructure, are available at: https://royalholloway.figshare.com/articles/Geospatial_Data/9205184. The post-earthquake satellite scene is available via Google Earth: https://www.google.com/earth/download/gep/agree.html, and via DigitalGlobe: https://discover.digitalglobe.com/. Sentinel 2B data can be downloaded from the Copernicus Open Access Hub: https://scihub.copernicus.eu/dhus/#/home. TanDEM-X 90 m data can be downloaded via the German Aerospace Centre: (https://geoservice.dlr.de/web/dataguide/tdm90/), and the application page for ~12 m data is: https://tandemx-science.dlr.de/cgi-bin/wcm.pl?page=TDM-Proposal-Submission-Procedure.

## References


51. *Digital Globe* (accessed 25 November 2018); http://worldview4.digitalglobe.com/#/main

52. Sheppard, S. R. J. & Cizek, P. The ethics of Google Earth: Crossing thresholds from spatial data to landscape visualisation. *J. of Env. Managem.* **90,** 2102-2117 (2009).

53. *European Space Agency Sentinel Online* (accessed 25 November 2018); https://sentinel.esa.int/web/sentinel/missions/sentinel-2

623 54. Hajnsek, I. et al. TanDEM-X: TanDEM-X Digital Elevation Models Announcement of
624 Opportunity; TD-PD-AO-0033 (*German Aerospace Center, Microwaves and Radar*
625 *Institute, Weßling*, 2016).
626 55. Potere, D. Horizontal positional accuracy of Google Earth's high-resolution imagery
627 archive. *Sensors* **8,** 7973–7981 (2008).
628 56. Mohammed, N. Z., Ghazi, A. & Mustafa, H. E. Positional accuracy testing of Google
629 Earth. *Int. J. of Multidiscipl. Sci & Eng*. **4,** 6-9 (2013).
630 57. Pulighe, G., Baiocchi, V. & Lupia, F. Horizontal accuracy assessment of very high
631 resolution Google Earth images in the city of Rome, Italy. *Int. J. of Dig. Earth* **9,** 342-362
632 (2016).
633 58. Benker, S. C., Langford, R. P. & Pavilis, T. L. Positional accuracy of the Google Earth
634 terrain model derived from stratigraphic unconformities in the Big Bend region, Texas,
635 USA. *Geocarto Int.* **26,** 1–13 (2011).
636 59. Youssef, A. M., Maerz, N. H. & Hassan, A. M. Remote sensing applications to geological
637 problems in Egypt: case study, slope instability investigation, Sharm El-Sheikh/Ras-
638 Nasrani area, southern Sinai. *Landslides* **6,** 353-360 (2009).
639 60. Stumpf, A., Lampert, T. A., Malet, J.-P. & Kerle, N. Multi-scale line detection for
640 landslide fissure mapping (*IEEE International Geoscience and Remote Sensing*
641 *Symposium*, Munich, 2012).
642 61. Parise, M. Observation of surface features on an active landslide, and implications for
643 understanding its history of movement, *Nat. Haz. Ear. Syst. Sci*. **3,** 569-580 (2003).
644 62. Stumpf, A., Malet, J.-P., Kerle, N., Niethammer, U. & Rothmund, S. Image-based
645 mapping of surface fissures for the investigation of landslide dynamics. *Geomorph*. **186,**
646 12-27 (2013).

63. Fleming, R. W. & Johnson, A. M. Structures associated with strike-slip faults that bound landslide elements. *Eng. Geol*. **27,** 39-114 (1989).

64. Krauskopf, K. B., Feitler, S. & Griggs, A. B. Structural Features of a Landslide near Gilroy, California. *The J. of Geol*. **47,** 630-648 (1939).

65. Stumpf, A., Malet, J.-P., Puissant, A. & Travelletti, J. in: *Land Surface Remote Sensing and Risks*, (Elsevier, London, 2016).

66. Avouac, J.-P., Ayoub, F., Leprince, S., Konca. O. & Helmberger, D. V. The 2005 Mw 7.6 Kashmir earthquake: Sub-pixel correlation of ASTER images and seismic waveforms analysis. *Ear. Planet. Sci. Lett*. **249,** 514-528 (2006).

67. Tamkuan, N. & Nagai, M. Fusion of multi-temporal interferometric coherence and optical image data for the 2016 Kumamoto earthquake damage assessment. *ISPRS Int. J. of Geo-Info*. **6,** 188 (2017).

68. Sims, J. D. & Garvin, C. D. Recurrent liquefaction induced by the 1989 Loma Prieta earthquake and 1990 and 1991 aftershocks: Implications for paleoseismicity studies. *Bull. of the Seismol. Soc of Am*. **85,** 51-65 (1995).

69. Cubrinovski, M. et al. Liquefaction effects and associated damages observed at the Wellington CenrePort from the 2016 Kaikoura earthquake. *Bull. of New Zeal. Soc. for Earthquake Eng*. **50,** 152-173 (2017).

70. Quigley, M. C., Bastin, S. & Bradley, B. A. Recurrent liquefaction in Christchurch, New Zealand, during the Canterbury earthquake sequence. *Geology* **41,** 419-422 (2013).

71. Wotherspoon, L. M., Pender, M. J. & Orense, R. P. Relationship between observed liquefaction at Kaiapoi following the 2010 Darfield earthquake and former channels of the Waimakariri River. *Eng. Geol*. **125,** 45-55 (2012).

72. Cubrinovski, M. et al. Soil liquefaction effects in the Central Business District during the February 2011 Christchurch Earthquake. *Seis. Res. Lett*. **82,** 893-904 (2011).

672 73. Hotelling, H. Analysis of a complex of statistical variables into principal components. *J.*
673 *of Educ. Psych.* **24,** 417-441 (1933).
674 74. Sharma, S. K., Gajbhiye, S. & Tignath, S. Application of principal component analysis in
675 grouping geomorphic parameters of a watershed for hydrological modelling. *Appl. Water*
676 *Sci*. **5,** 89-96 (2015).
677 75. Qi, J. et al. A modified soil adjusted vegetation index. *Remote. Sens. Environ*. **48,** 119-
678 126 (1994).
679

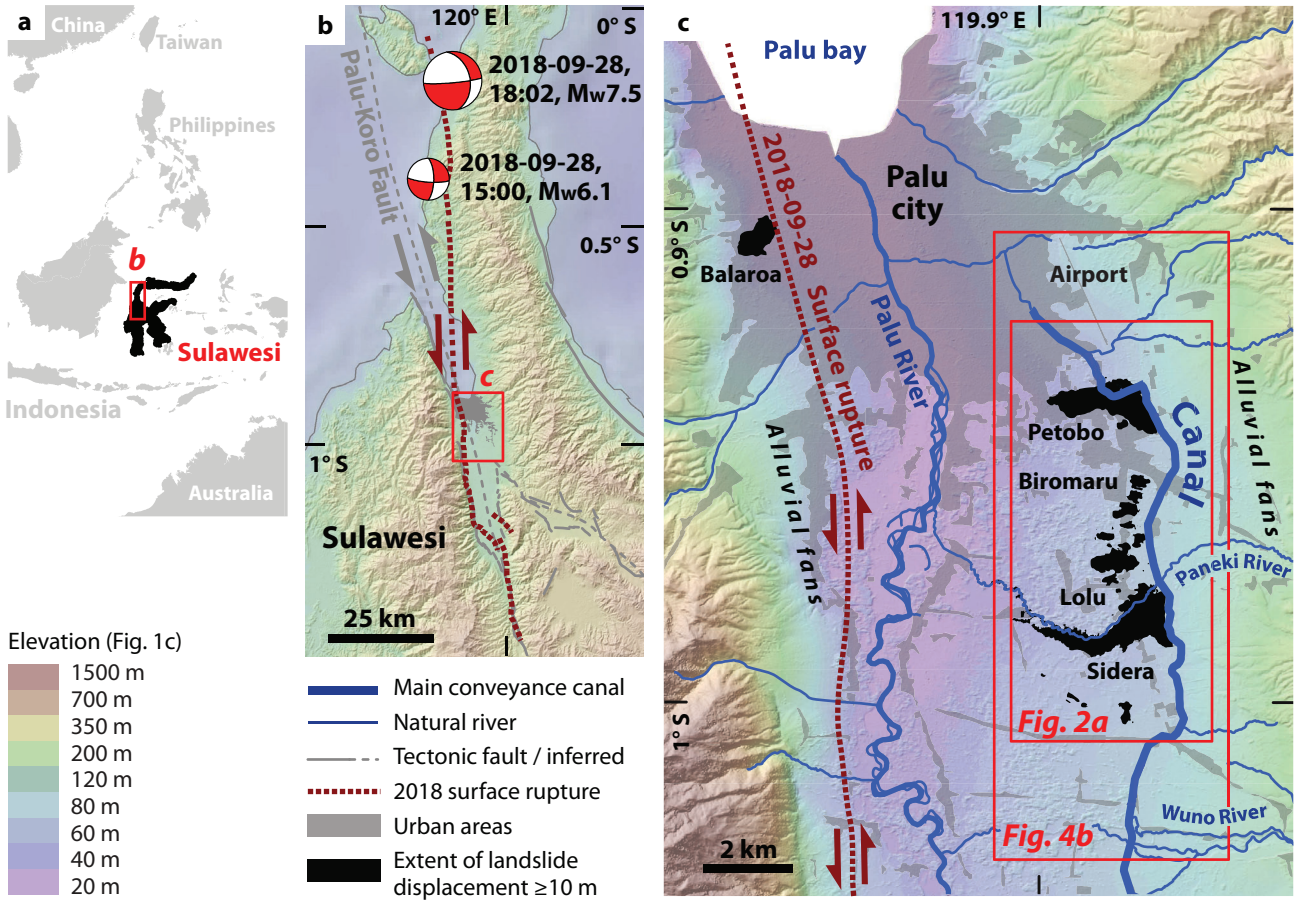
a
China
Taiwan
Philippines
b
Sulawesi
Indonesia
Australia
b
120° E
0° S
2018-09-28, 18:02, Mw7.5
2018-09-28, 15:00, Mw6.1
Palu-Koro Fault
0.5° S
c
1° S
Sulawesi
25 km
c
119.9° E
Palu bay
2018-09-28 Surface rupture
Palu city
S 0.9°
Balaroa
Airport
Palu River
Petobo
Biromaru
Canal
Alluvial fans
Paneki River
Lolu
Sidera
Fig. 2a
Fig. 4b
Wuno River
S 1°
2 km
Elevation (Fig. 1c)
1500 m
700 m
350 m
200 m
120 m
80 m
60 m
40 m
20 m
Main conveyance canal
Natural river
Tectonic fault / inferred
2018 surface rupture
Urban areas
Extent of landslide displacement ≥10 m

**Figure 1**

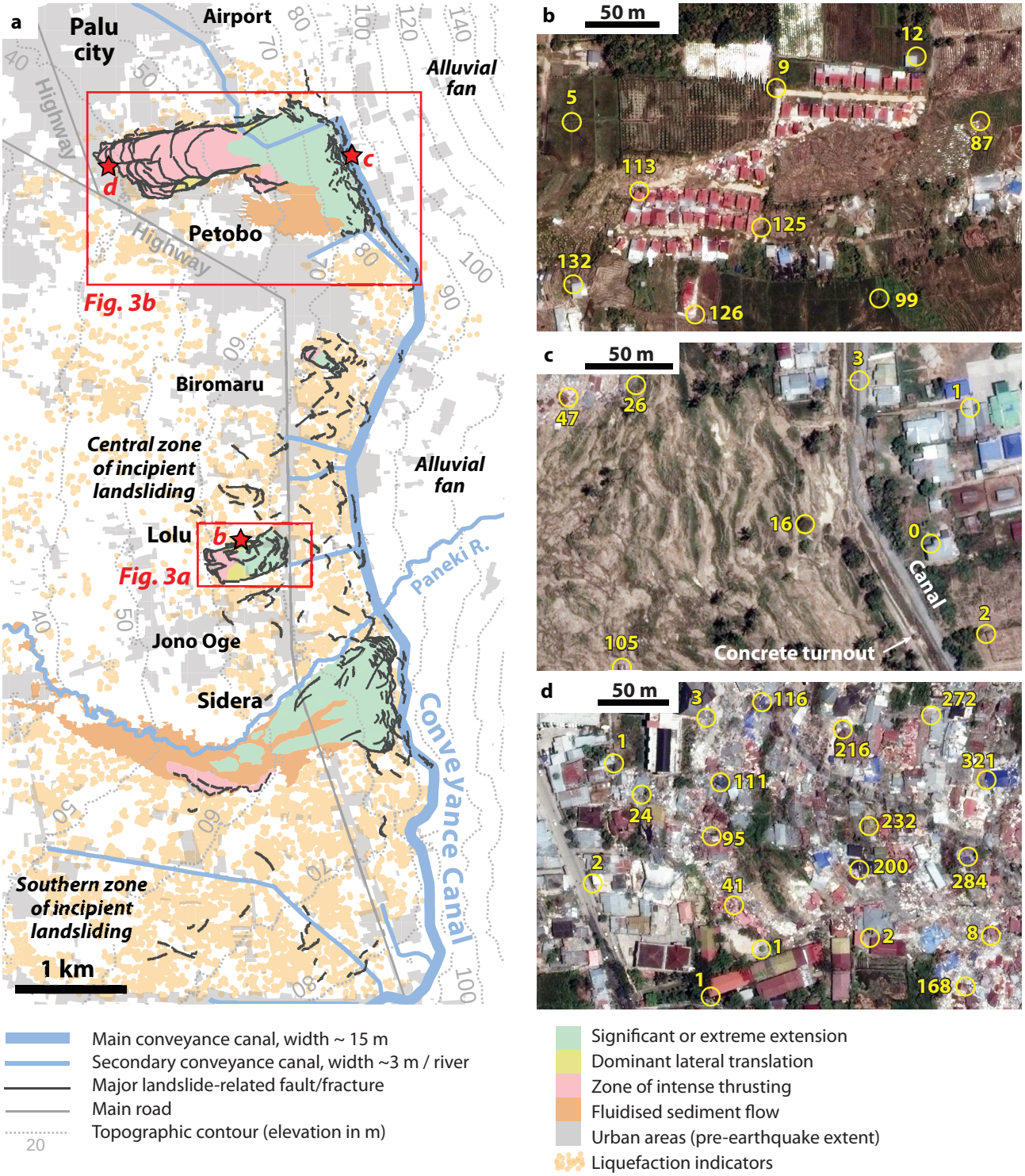
a
Palu city
Airport
Alluvial fan
Highway
Petobo
Fig. 3b
c
d
Biromaru
Central zone of incipient landsliding
Alluvial fan
Lolu
b
Fig. 3a
Paneki R.
Jono Oge
Sidera
Conveyance Canal
Southern zone of incipient landsliding
1 km
b
50 m
12
9
5
87
113
125
132
99
126
c
50 m
3
47
26
1
16
0
Canal
2
105
Concrete turnout
d
50 m
3
116
272
1
216
321
111
24
232
95
2
200
284
41
1
2
8
1
168
Main conveyance canal, width ~ 15 m
Secondary conveyance canal, width ~3 m / river
Major landslide-related fault/fracture
Main road
Topographic contour (elevation in m)
20
Significant or extreme extension
Dominant lateral translation
Zone of intense thrusting
Fluidised sediment flow
Urban areas (pre-earthquake extent)
Liquefaction indicators

**Figure 2**

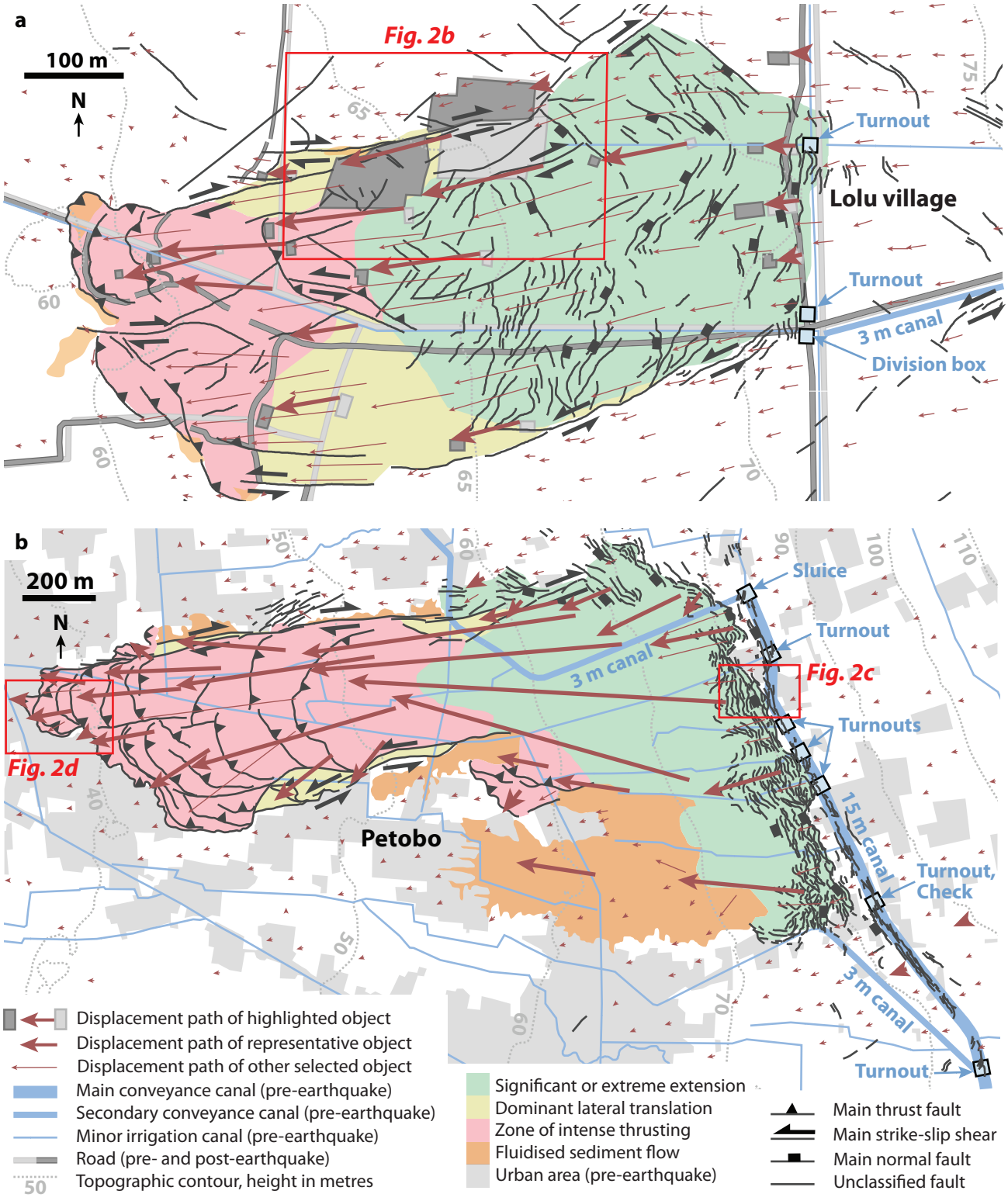
a
100 m
N
Fig. 2b
Turnout
Lolu village
Turnout
3 m canal
Division box
b
200 m
N
Fig. 2d
Sluice
Turnout
3 m canal
Fig. 2c
Turnouts
1.5 m canal
Turnout, Check
3 m canal
Turnout
Petobo
Displacement path of highlighted object
Displacement path of representative object
Displacement path of other selected object
Main conveyance canal (pre-earthquake)
Secondary conveyance canal (pre-earthquake)
Minor irrigation canal (pre-earthquake)
Road (pre- and post-earthquake)
Topographic contour, height in metres
Significant or extreme extension
Dominant lateral translation
Zone of intense thrusting
Fluidised sediment flow
Urban area (pre-earthquake)
Main thrust fault
Main strike-slip shear
Main normal fault
Unclassified fault

**Figure 3**

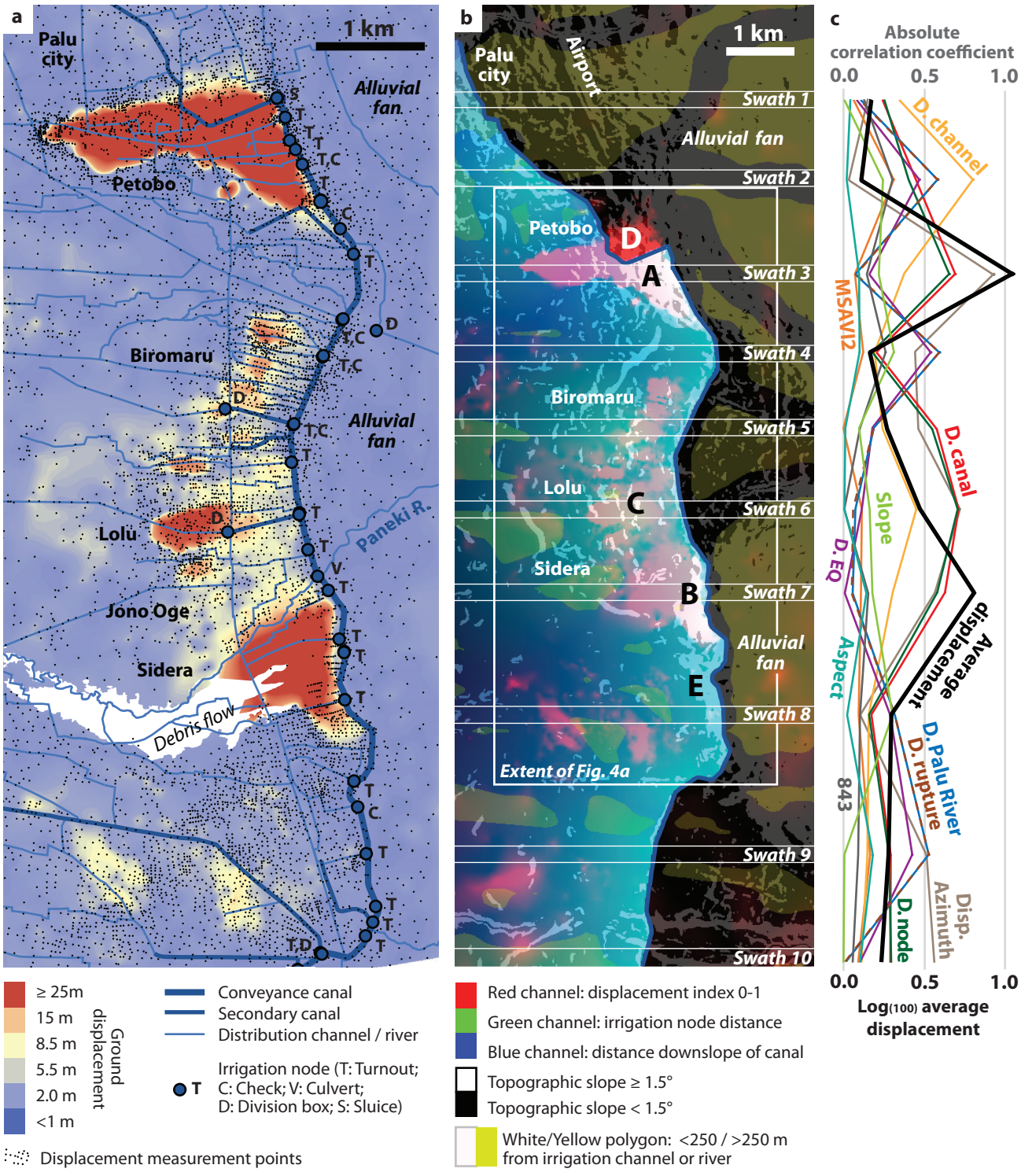
a
Palu city
1 km
Alluvial fan
Petobo
Biromaru
Alluvial fan
Lolu
Paneki R.
Jono Oge
Sidera
Debris flow
≥ 25m
15 m
8.5 m
5.5 m
2.0 m
<1 m
Ground displacement
Conveyance canal
Secondary canal
Distribution channel / river
T
Irrigation node (T: Turnout; C: Check; V: Culvert; D: Division box; S: Sluice)
Displacement measurement points
b
Palu city
Airport
1 km
Swath 1
Alluvial fan
Swath 2
Petobo
D
A
Swath 3
Swath 4
Biromaru
Swath 5
Lolu
C
Swath 6
Sidera
B
Swath 7
Alluvial fan
E
Swath 8
Extent of Fig. 4a
Swath 9
Swath 10
Red channel: displacement index 0-1
Green channel: irrigation node distance
Blue channel: distance downslope of canal
Topographic slope ≥ 1.5°
Topographic slope < 1.5°
White/Yellow polygon: <250 / >250 m from irrigation channel or river
c
Absolute correlation coefficient
0.0
0.5
1.0
D. channel
MSAVI2
D. canal
Slope
D. EQ
Aspect
Average displacement
D. Palu River
D. rupture
843
Disp. Azimuth
D. node
0.0
0.5
1.0
Log(100) average displacement

**Figure 4**